AIAA JOURNAL
Vol. 44, No. 12, December 2006

Experimental Investigation of Separation Control Part 2: Zero Mass-Flux Oscillatory Blowing

David Greenblatt,* Keith B. Paschal,† Chung-Sheng Yao,‡ and Jerome Harris§
NASA Langley Research Center, Hampton, Virginia 23681-2199

DOI: 10.2514/1.19324

The control of a separated flow over a wall-mounted hump, by means of two-dimensional zero mass-flux perturbations, was studied experimentally to generate a data set for the development and evaluation of computational methods. The companion paper (Part 1) considered details of the baseline (uncontrolled) case and a steady-suction control case. The data set for a specific zero mass-flux control case comprised static surface pressures together with phase-averaged unsteady surface pressures and particle image velocimetry flowfield measurements. Additional surface pressures were acquired for a variety of control frequencies, control amplitudes and Reynolds numbers. Due consideration was given to characterizing the flow in the vicinity of the control slot, with and without external flow, and to perturbation two-dimensionality. Triple-decomposition of the fluctuating velocity and pressure fields was employed for presenting and analyzing the experimental data. This facilitated an assessment of the mechanism of separation control and the quantification of the coherent and turbulent surface pressures, Reynolds stresses, and energy fluxes. Spanwise surface pressures and phase-averaged stereoscopic particle image velocimetry data revealed an effectively two-dimensional flowfield despite highly three-dimensional instantaneous flow structures.

Nomenclature

A	=	projected model area, $s \times c$
b	=	model slot width
C_{Dp}	=	model form drag coefficient
C_Q	=	volumetric flux coefficient, $u_s b/U_\infty c$
C_P	=	time-mean pressure coefficient
C_μ	=	either steady flow momentum coefficient, $\rho_J U_J^2 b/(1/2\rho_\infty U_\infty^2 c)$ or oscillatory flow momentum coefficient, $2b\overline{\tilde{u}_J^2}/(cU_\infty^2)$
c	=	model chord length
F^+	=	reduced excitation frequency, $f_e X/U_\infty$
f_e	=	excitation frequency
g	=	any fluctuating quantity
H	=	distance between model base and tunnel ceiling
h	=	model height
M	=	Mach number
N	=	number of PIV image pairs
P, $\tilde{p}$, p'	=	time-mean, coherent, and turbulent surface pressure
Q	=	suction flow rate
q	=	dynamic pressure
Re	=	Reynolds number based on model chord length
Re_θ	=	Reynolds number based on momentum thickness
s	=	model span
T	=	time over which time-averaging is performed
U, V, W	=	time-mean velocities in directions x, y, z; also U_i, $i = 1, 2, 3$
U_J	=	slot mean velocity
U_ϕ	=	phase velocity
u', v', w'	=	turbulent velocity fluctuations in directions x, y, z; also u_i', $i = 1, 2, 3$
$\tilde{u}$, $\tilde{v}$, $\tilde{w}$	=	coherent velocity fluctuations in directions x, y, z; also $\tilde{u}_i$, $i = 1, 2, 3$
u_J	=	slot velocity
$\tilde{u}_J$	=	oscillatory component of slot velocity
u_p	=	slot peak-blowing velocity
u_s	=	slot suction velocity
X	=	baseline (no flow control) distance from the slot to flow reattachment point
X_R	=	distance from the slot to flow reattachment
x, y, z	=	coordinate directions measured from the model leading edge
θ	=	boundary layer momentum thickness
λ	=	wavelength
ξ	=	streamwise coordinate measured from the slot
ρ	=	air density
ϕ	=	phase angle
ψ	=	cross-stream coordinate measured from the slot
$\langle\ \rangle$	=	denotes phase-averaging
$*$	=	denotes root mean square

Subscript

∞	=	freestream conditions

Presented as Paper 0485 at the 43rd AIAA Aerospace Sciences Meeting and Exhibit, Reno, NV, 10–13 January 2005; received 3 August 2005; revision received 11 January 2006; accepted for publication 27 January 2006.

*NRC Research Associate, Flow Physics & Control Branch, Mail Stop 170; currently Research Scientist, Hermann Foettinger Institute for Fluid Mechanics, Technical University of Berlin, 8 Mueller Breslau Street, D-10623 Berlin, Germany; david.greenblatt@pi.tu-berlin.de. Senior Member AIAA.

†Aerospace Engineer, Flow Physics & Control Branch, Mail Stop 170. Member AIAA.

‡Aerospace Engineer, Flow Physics & Control Branch, Mail Stop 170.

§Optical Engineering Technician, Flow Physics & Control Branch, Mail Stop 170.

I. Introduction

SEPARATION control by means of zero mass-flux and nonzero mass-flux oscillatory jets is known to be effective in a variety of incompressible flows under varied conditions [1]. Control is particularly effective when the perturbations are introduced in a two-dimensional manner, for example, at the leading edge of a wing or at the shoulder of a deflected flap. It is believed that large spanwise structures in the flow are responsible for momentum transfer across the boundary layer and, in so doing, delay separation. Present-day CFD methods appear capable of predicting trends associated with controlled flows [2], but there are no known techniques that can adequately calculate the effect of leading parameters such as reduced

frequency and perturbation amplitude. This is partly due to the complex nature of the flow, where turbulence and coherent motion coexist, whereas the correct imposition of control boundary conditions also poses significant challenges. Because of the increased technological importance of controlled flows, there is an urgent need to develop CFD methods with a predictive capability. Present attempts to develop such methods are hampered in one way or another by incomplete data sets, uncertain or undocumented inflow and boundary conditions, or inadequate flowfield measurements.

This paper is the second part of a low-speed experimental investigation studying the control of a separated flow region, formed over the ramp of a wall-mounted hump model, for the express purpose of generating a data set for the development and evaluation of computational methods. The first part of this investigation considered the case with no control applied (baseline) and the case with control applied via steady suction from a two-dimensional slot [3]. The specific objective of this second part was to provide a data set corresponding separation control by means of zero mass-flux oscillatory blowing. Both parts of the investigation formed part of a CFD validation workshop sponsored by NASA Langley Research Center, in association with the U.S. Air Force Office of Scientific Research, the European Research Community on Flow, Turbulence, and Combustion, the International Association of Hydraulic Engineering and Research, QNET-CFD, and the National Institute of Aerospace. The present case was referred to as "Case 3" of the workshop [2]. Note, however, that Case 3 comprises three separate subcases in all, namely, the baseline and suction cases detailed in Part 1 [3], and the zero mass-flux case described here. Nevertheless, baseline pressure and flowfield data were reacquired here for purposes of consistency and completeness.

For the present data set, a single zero mass-flux test case was selected, i.e., a specific control perturbation frequency and amplitude. This test was subjected to detailed surface pressure and flowfield measurements. Additional surface pressure data were acquired at various perturbation reduced frequencies and amplitudes and Reynolds numbers. This was done to facilitate additional computations for control under various conditions and to illustrate consistency of the data set.

II. Scope & Layout

This investigation is introduced by means of a brief description of the setup, range of measurements, and criteria motivating the control test case selection (Sec. III). This is followed by a discussion of the slot calibration and how it is used to quantify the zero mass-flux boundary condition (Sec. IV). The main section of this paper (Sec. V) provides a framework for decomposing the velocity and pressure fields and subsequent presentation of the data. As a CFD test case, the discussion is geared mainly towards consistency and reliability, rather than detailed analysis of the data. Nevertheless, due consideration is given to seemingly anomalous aspects of control, effects of Reynolds number, reduced frequency, reduced amplitude, generation and formation of the controlling large coherent structures (LCSs), surface pressure waves, coherent and turbulent flowfield statistics, and two-dimensionality.

III. Experimental Setup

A full description of the experimental setup was provided previously [3] and thus only a pertinent summary is presented here. The setup consisted of a wall-mounted modified Glauert hump model (height h and chord length c), located between two glass endplates. The leading and trailing edges of the model were faired smoothly with a wind tunnel splitter plate (see Fig. 1). A spanwise slot located at the $x/c = 65\%$ was used for separation control. This assembly was installed in the open-return NASA Langley shear flow tunnel and tested under both baseline and controlled conditions for $Re \leq 1,114,800$ and $M \leq 0.12$; deviations from the nominal Re and M values never varied by more than 1%. The model was equipped with 165 streamwise and spanwise static pressure ports and

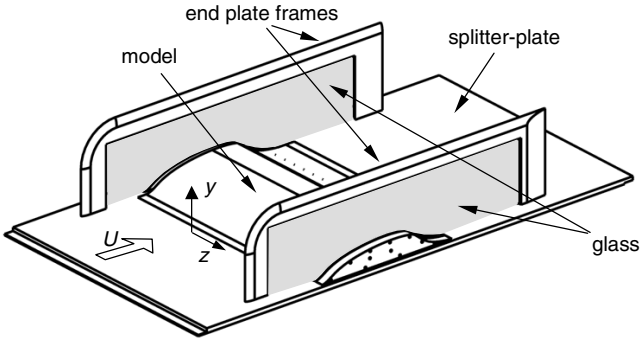

Fig. 1 Perspective view of experimental setup, showing the model, endplates, and splitter plate.

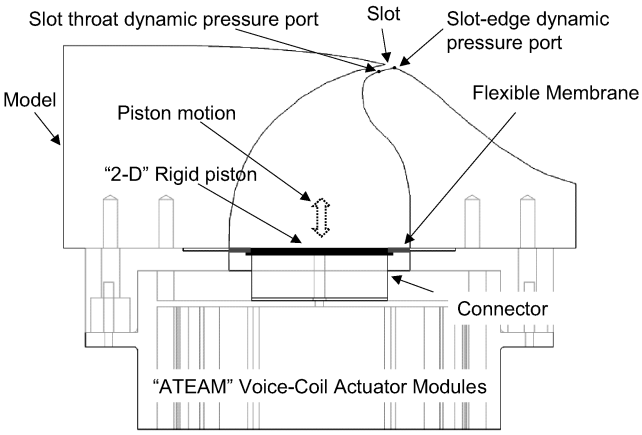

Fig. 2 Side-view schematic showing the voice-coil actuator and piston assembly mounted adjacent to the plenum beneath the model.

20 unsteady pressure ports in the separated flow region. In addition to the unsteady pressure ports in the separated region, unsteady pressure measurements were made within the throat of the slot and on the downstream slot edge (see Fig. 2). The former was used to quantify the control "delivery rms pressure" (see Sec. IV); the latter was used to establish a fluctuating pressure boundary condition that was used for comparing and analyzing downstream unsteady pressure data (see Sec. V).

Separation control was achieved using zero mass-flux oscillatory blowing introduced from the spanwise slot, where careful attention was paid to maintaining slot-flow two-dimensionality. This was achieved by means of a rigid piston, spanning the model, that was secured to the base of the plenum by means of a flexible membrane and flange (Fig. 2). The piston was driven externally by six voice-coil-based actuator modules [aero and thermally engineered actuator modules (ATEAM) actuators designed and manufactured by J. Kiedaisch, H. Nagib and their associates from the Illinois Institute of Technology (IIT) [4], providing maximum slot velocities of approximately 80 m/s at frequencies ranging from 60 to 500 Hz. An O-ring maintained an airtight seal between the actuator flange and the base of the plenum. The slot flow was calibrated and characterized for both tunnel flow-off (quiescent) and flow-on (nonquiescent) conditions, using hot-wire anemometry, throat dynamic pressure measurements, and two-dimensional particle image velocimetry (PIV) (see Secs. IV and V). The "inflow" turbulent velocity profile at $x/c = -2.14$ was documented using a pitot probe and hot-wire anemometer, with $\delta/h = 0.46$ and $Re_\theta = 5,700$ (see [3] for more details). This inflow boundary layer was approximately 20% thinner than that measured with the suction manifold in place. Consequently, baseline pressure and flowfield data for the baseline case were reacquired so as to provide baseline data consistent with the inflow profile.

For purposes of CFD validation, a single test case was selected ($u_p = 26.6$ m/s; $f_e = 138.5$ Hz) and detailed phase-dependent

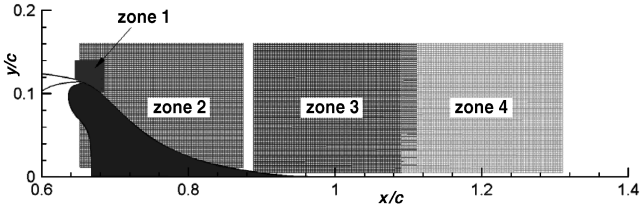

Fig. 3 Schematic of the ramp showing the four zones in which baseline and phase-resolved two-dimensional PIV measurements were acquired.

flowfield measurements were made using two-dimensional and stereoscopic PIV. The specific test case conditions (control frequency and amplitude) were selected based on the following three criteria: 1) the peak slot velocity should be of a similar magnitude to the suction slot velocity studied previously [3]; 2) perturbations should exert substantial, but not excessive, control of the separated region; and 3) dimensionless control parameters should correspond to a specific case already tested under cryogenic conditions [5,6]. The rationale behind these criteria was to 1) facilitate a comparison of the different control schemes, 2) avoid a fully attached flow on the ramp that is less challenging for CFD, and 3) allow a direct comparison with high Reynolds number (cryogenic) conditions. In addition to the test case, surface static and dynamic pressure measurements were made for a wide variety of perturbation control frequencies and amplitudes. Furthermore, a comparison of this data set with the cryogenic data set [5] provided an opportunity to assess the effect of Reynolds number (laboratory vs simulated flight conditions) on control, without the usual complicating effects of transition and compressibility.

For the baseline case and the control test case, two-dimensional PIV measurements were made in the four regions shown in Fig. 3. For the control test case, data were acquired and averaged at 36 phases of the control cycle. The selection of these regions was based on acquiring 1) high-resolution measurements in the near vicinity of the control slot (zone 1), and 2) flowfield data over the entire separated region (zones 2–4). Separate phase-resolved stereoscopic PIV data were acquired in planes perpendicular to the zones shown in Fig. 3, located at $x/c = 0.7$ and 1.0, corresponding to the spanwise region: $-0.12 < z/s < 0.12$ ($z/s = \pm 0.5$ denote the endplate locations).

IV. Zero Mass-Flux Boundary Condition: Slot Calibration

A. Background

A boundary condition for CFD validation that can reliably be considered to be two-dimensional presents a number of challenges, even when using an unquestionably zero mass-flux device. Firstly, verifying the fidelity of a device at a specific spanwise location via direct measurement (i.e., $Q(z) = 0$) is extremely difficult. Rapid oscillatory changes in flow direction, high instantaneous shear, zero-crossings, and near-wall complications introduce unacceptably high uncertainties to both hot-wire and optical measurement techniques.

Secondly, a zero mass-flux device presents a problem when one attempts to quantify it in the sense of a meaningful boundary condition, particularly when comparisons are to be made with steady blowing or suction. This difficulty stems from the duality of the device in the context of a traditional boundary condition: two-dimensional *steady* blowing is characterized by a momentum coefficient [7][‖]:

$$C_\mu = \frac{\rho_J u_J^2 b}{1/2 \rho_\infty U_\infty^2 c} \tag{1}$$

but steady slot suction is quantified by means of a volumetric flux coefficient:

$$C_Q = \frac{Q}{U_\infty L} = \frac{u_S b}{U_\infty c} \tag{2}$$

where the subscripts J and s refer to "blowing jet" and "suction slot" conditions, respectively. The former was demonstrated empirically [7] whereas the latter appears to have been borrowed from the analysis of homogeneous suction on a flap plate [8]. For unsteady slot flows, a common approach is to extend the standard momentum coefficient definition to include an oscillatory component: $u_J = U_J + \tilde{u}_J$ [9]. For a zero mass-flux ($C_Q = 0$) incompressible ($\rho_J = \rho_\infty$) oscillatory slot flow, the time-mean momentum coefficient can be written as

$$C_\mu = \frac{2b}{c} \frac{\overline{\tilde{u}_J^2}}{U_\infty^2} \tag{3}$$

from Eq. (1). This implicitly *assumes* that blowing and suction cycles introduce equal momentum to the flow. This may have some validity when the peak suction slot velocity is less than U_∞, but cannot be considered universally valid. Nevertheless, for the purpose of consistency with previous investigations, comparisons between different separation control methods are based either on C_μ or comparable slot velocities.

Finally, the generally accepted experimental approach to slot-flow characterization is to calibrate the slot under quiescent conditions, i.e., with $U_\infty = 0$ (tunnel-off) and then *assume* that this calibration remains valid under test conditions ($U_\infty \neq 0$) where the pressure and flowfield data are acquired. It was deemed necessary to directly establish the validity of this assumption.

B. Quiescent Environment Calibration

The near field of a steady two-dimensional jet consists of a laminar (or potential) core often termed a "top-hat" profile. On the other hand, steady suction through a slot produces a sink flow in its near vicinity [10]. In zero mass-flux oscillatory jets, the velocity profiles develop in a spatial and temporal manner, but the peak-blowing velocity near the slot is seen to be associated with a similar type of top-hat profile. Phase-averaged hot-wire data in and in the vicinity of the slot at $\psi = 0$ were acquired and divided into blowing and suction cycles ($\psi = 0$ is midway between the lower corner of the upper slot edge and the lower slot edge; see Fig. 4). Within the slot at $\xi < 1$, the probe introduced blockage and these data are not representative of the slot velocities. As the probe traverses out of the slot ($\xi > 1$) and the blockage effect reduces, the blowing peaks tend towards a constant value at the same phase whereas the suction peaks diminish. Plotting only the phase-averaged peak values shows that during the blowing cycle, the peak values (u_p) are virtually constant for $1.25 < \xi < 2.25$, whereas the suction peaks exhibit behavior similar to that of a sink flow (Fig. 4). Because of the sink-flow nature of the suction phase, these data have little value in the context of a slot calibration, because small changes in ξ result in relatively large changes in u_p. For CFD boundary condition requirements, all slot calibrations were based on

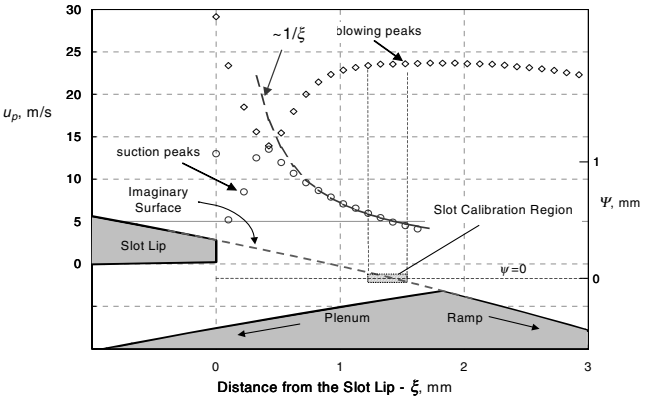

Fig. 4 Phase-averaged blowing and suction peaks from hot-wire measurements within slot at $\psi = 0$.

[‖]The active flow control *momentum coefficient* C_μ should not be confused with the closure coefficient commonly used in turbulence models.

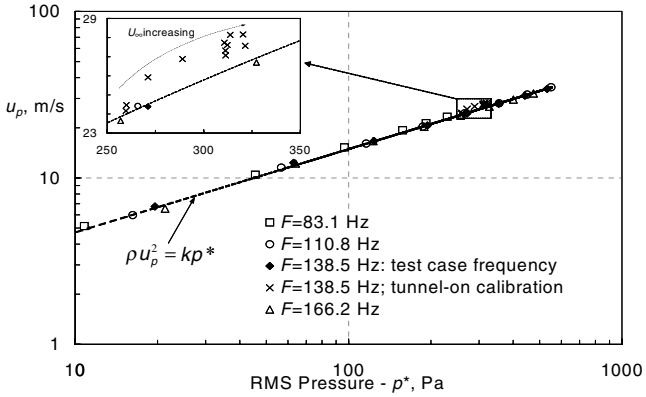

Fig. 5 Correlation of throat rms "deliver pressure" and phase-averaged peak-blowing velocities (quiescent and nonquiescent calibrations). Inset shows the effect of increasing U_∞ (linear scale).

the phase-averaged blowing peak velocities at the point where $\psi = 0$ intersects the virtual surface of the model. u_p was also found to be insensitive to small vertical changes ($\Delta\psi = \pm 50\ \mu$m; hatched section in Fig. 4). This facilitated periodic health monitoring of the actuator and assessment of perturbation two-dimensionality (Sec. IV.C).

The nature of the peak velocities described here was shown to be similar for different frequencies and amplitudes tested. In addition, unsteady throat pressures (see Fig. 2) were recorded simultaneously. A summary of the throat delivery rms pressure $p^* = \sqrt{\tilde{p}^2}$ vs u_p is shown in Fig. 5 and indicates a useful Bernoulli-type relationship:

$$\tfrac{1}{2}\rho u_p^2 = kp^* \qquad (k = 1.31) \tag{4}$$

that is independent of forcing frequency.

C. Perturbation Two-Dimensionality

The identification of a core region with approximately constant peak velocity allowed convenient examination of the slot two-dimensionality. Data were acquired at three locations on either side of the model centerline covering approximately the central 50% of the model, for $f_e = 138.5$ Hz and five different throat rms pressures p^* (Fig. 6a). The blowing peaks are shown to be approximately constant along the span, although the peak velocities at $z/s > 0$ are slightly larger than those at $z/s < 0$. The main reason for this is the nonuniformity of the spanwise slot width that varies from 0.79 to 0.74 mm. If we account for this and plot bu_p (i.e., peak Q/s), the asymmetry is effectively eliminated (Fig. 6b). It should be noted, however, that the slot nonuniformity results in a small momentum boundary condition asymmetry. Small effects of the slot nonuniformity were also evident in the cases involving steady suction, where the pressure recoveries were slightly larger for $z/s < 0.5$ (see [3]).

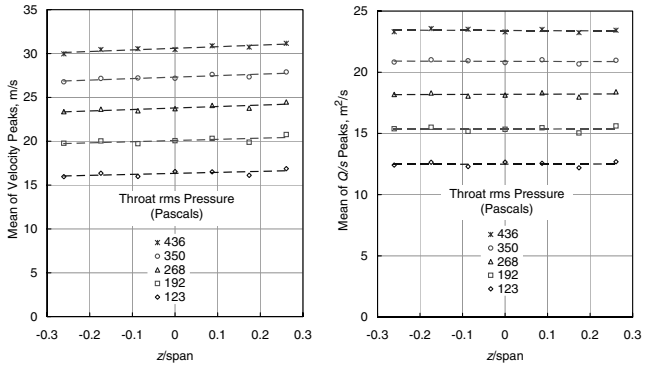

Fig. 6 Spanwise measurements of phase-averaged a) peak-blowing velocities and b) phase-averaged peak-blowing mass-flux.

D. Nonquiescent Calibration

To assess the effect of freestream velocity on the application of the boundary condition, two approaches were adopted. The first was to conduct hot-wire measurements in the core region of the slot and the second involved high-resolution phase-averaged PIV measurements in the vicinity of the slot jet. The former is discussed here and the latter is discussed in Sec. V.

The effect of increasing U_∞ from zero to test conditions on the p^* vs u_p relationship [Eq. (4)] is shown in Fig. 5 (see the inset for greater detail). With increasing freestream velocity, in general both the p^* and u_p increase due to broadband vortex shedding and Eq. (4) retains its validity. Thus, the quiescent calibration relationship [Eq. (4)] can be used directly to establish nonquiescent boundary conditions. It may be concluded that accurate establishment of a slot boundary condition requires a representative unsteady pressure measurement in the throat of the slot.

To quantify the CFD boundary condition in dimensionless terms and allow comparison with other investigations, it was assumed that $\overline{\tilde{u}_J^2} = u_p^2/2$ (i.e., a purely sinusoidal oscillatory flow) and thus from Eqs. (3) and (4),

$$C_\mu = \frac{b}{c}\frac{kp^*}{q_\infty} \tag{5}$$

where p^* data were acquired simultaneously with surface pressure and flowfield data. The principal source of error was considered to be bias, with $\Delta u_p/u_p \le 3.5\%$ ($\Delta C_\mu/C_\mu \le 7\%$). The dimensionless control frequency was defined as

$$F^+ = \frac{f_e X}{U_\infty} \tag{6}$$

where X is the distance from the slot to the baseline reattachment line.

V. Pressure & Flowfield Data

A. Triple Decomposition

For the purposes of presenting and analyzing the experimental data, all fluctuating quantities $g(x,t)$ were decomposed according to the so-called triple decomposition [11,12]:

$$g(x,t) = G(x) + \tilde{g}(x,t) + g'(x,t) \tag{7}$$

where

$$G(x) \equiv \overline{g(x)} = \lim_{T\to\infty}\frac{1}{T}\int_0^T g(x,t)\,\mathrm{d}t \tag{8}$$

$\tilde{g}(x,t)$ is the purely periodic component and $g'(x,t)$ is the random turbulent component. Experimental data were generally acquired by means of phase averaging:

$$\langle g(x,t)\rangle = \lim_{N\to\infty}\sum_{n=1}^{N} g(x, t+n\tau) \tag{9}$$

where

$$\tilde{g}(x,t) = \langle g(x,t)\rangle - G(x) \tag{10}$$

and thus

$$g(x,t) = \langle g(x,t)\rangle + g'(x,t) \tag{11}$$

The triple decomposition aids in understanding the interaction between the coherent and incoherent components of the flowfield and facilitates quantification of the energy fluxes between the mean, coherent and random fields [13]. For the surface static and unsteady pressure data: $TU_\infty/c \ge 5000$; for the two-dimensional and stereoscopic PIV data: $400 \le N \le 2000$. Full details of the PIV setup as well as bias, resolution, and precision errors (based on 95%

Table 1 Maximum bias, resolution, and precision error estimates for pressure and velocity measurements [14,15]

Measured quantity	Bias or resolution	Precision
C_p	0.003	0.008
C_p'	0.001	0.001
U/U_∞, V/U_∞	1.3%	1%
W/U_∞	−3%	1%
$\overline{uu}/U_\infty^2$, $\overline{vv}/U_\infty^2$, $\overline{uv}/U_\infty^2$	0.02%	13%, 13%, 17%

confidence intervals) can be found in [3] and a summary is shown in Table 1 [14,15].

B. Pressure & Flowfield Data

Time-mean and rms pressure coefficients for the baseline and zero mass-flux test cases are shown in Figs. 7a and 7b in the separated flow zone; corresponding $U(x, y)$ contours are shown in Figs. 8a and 8b, respectively (zero mass-flux controlled profiles were obtained by time averaging the 36 phase-averaged profiles). C_p data for steady suction at $u_s \approx u_p$, corresponding to the suction test case described in Part 1 of this paper , are also shown in Figs. 7a and 7b for purposes of comparison. For the baseline case, separation and reattachment occur at $x/c \approx 0.67$ (Fig. 10e) and $x/c \approx 1.11$ (Fig. 8a), respectively. Unlike the steady-suction case, zero mass-flux control results in a relatively small effect on the pressure immediately upstream of the slot. Downstream of the slot, the separation point is not significantly affected (also see PIV data below) but there is a relatively sharp pressure drop, followed by a recovery that crosses over the baseline data. This results in a curious situation where control appears to promote separation close to the control location while simultaneously shortening the reattachment length. This is consistent with high Reynolds number observations [5], but the C_μ values were much less than those shown here (see further discussion in Sec. V.C).

As a consequence of the triple decomposition, we can define a periodic rms pressure coefficient

$$C_{\tilde{p}}^* = \sqrt{\overline{\tilde{p}^2}}/q_\infty \tag{12}$$

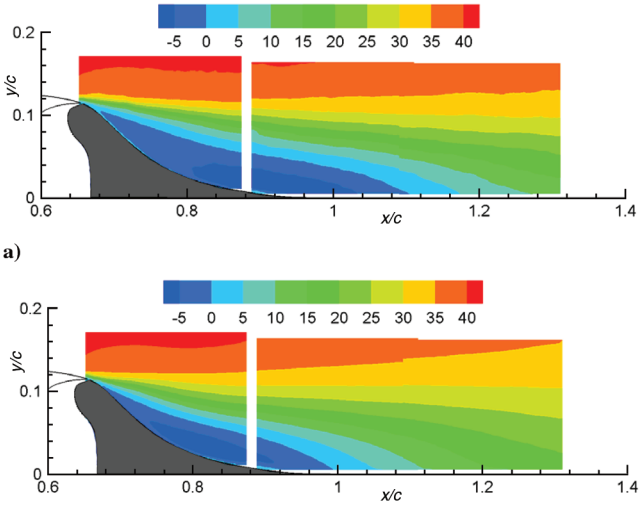

Fig. 8 a) Baseline streamwise velocity contours (m/s) in the separated flow region. b) Controlled ($F^+ = 0.77$, $C_\mu = 0.11\%$) time-mean streamwise velocity contours (m/s) in the separated flow region.

and a turbulent rms pressure coefficient

$$C_{p'}^* = \sqrt{\overline{p'^2}}/q_\infty \tag{13}$$

[see Eq. (7)]. In the context of CFD validation using, for example, URANS-type approaches, $C_{\tilde{p}}^*$ can be directly compared with computed pressure fluctuations. Over the separated region, the turbulent pressure fluctuations associated with zero mass-flux control are significantly larger than those of the baseline and suction cases (Fig. 7b). It is interesting to note that fluctuating turbulence peaks occur slightly upstream of reattachment for both the baseline ($x/c = 1.11$; cf. Fig. 8a) and control ($x/c = 0.98$; cf. Fig. 8b) cases. For uncontrolled reattaching flows, peak wall pressure fluctuations are often used as an estimate of the reattachment line; the same was seen to be true for steady suction [3]. It is therefore of some interest

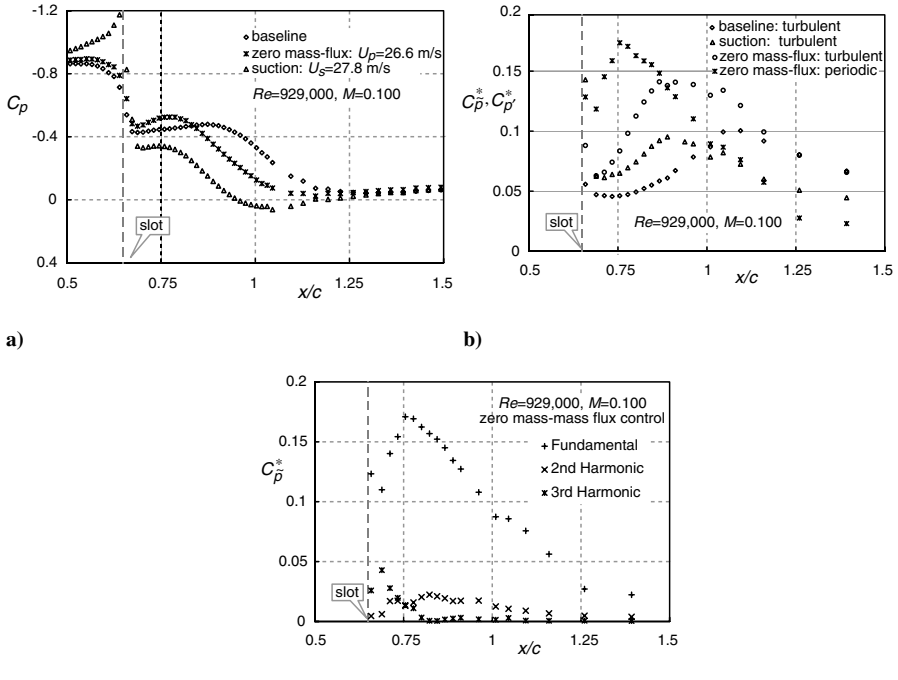

Fig. 7 a) Baseline and controlled mean surface pressures on the model surface. b) Baseline and controlled fluctuating surface pressures on the model surface (zero mass-flux control corresponds to $F^+ = 0.77$, $C_\mu = 0.11\%$). c) Harmonic components of controlled fluctuation surface pressures.

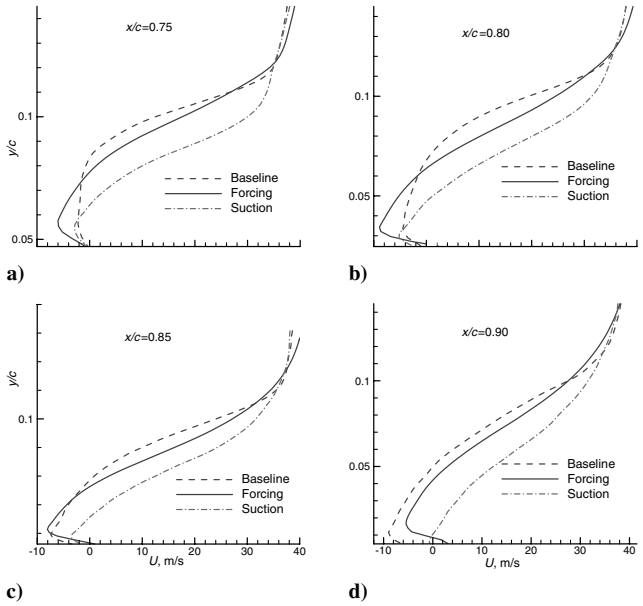

Fig. 9 Velocity profiles on the ramp corresponding to baseline and time-mean controlled scenarios.

that a similar observation is made for the control case when the coherent pressure fluctuations are extracted. It also appears that the peak $C_{p'}^*$ location scales with the maximum $\mathrm{d}C_P/\mathrm{d}x$ (cf. [16]). In the immediate vicinity downstream of the slot, $C_{\tilde{p}}^*$ far exceeds $C_{p'}^*$ and this is consistent with greater coherence relative to turbulence associated with the traveling pressure waves. The periodic pressure coefficient can further be decomposed into its Fourier components (Fig. 7c). It is seen that the pressure perturbation at the excitation frequency (fundamental) dominates throughout the separated and reattaching flow region.

Comparing Figs. 7a and 7c, we note that the region in which separation is *promoted* ($0.67 \lesssim x/c \lesssim 0.77$) is associated with amplification of the fundamental coherent pressure wave; the region of pressure recovery ($x/c \gtrsim 0.77$) is associated with its dissipation.

Further insight into the time-mean nature of control can be obtained by comparing velocity profiles $U(x, y)$ in the separated region (Figs. 9a–9d; extracted from Figs. 8a and 8b); suction test case data [3] are also shown for purposes of comparison. Downstream of the slot at $x/c = 0.75$ (Fig. 9a), control increases the momentum in the outer part of the shear layer (discussed further later in this paper), but the reverse flow velocities near the wall increase substantially, thereby generating a shallower but stronger recirculation region (or bubble). With increasing x/c this recirculation region strengthens, as can be seen by the increasing disparity between the outer layer and inner layer profiles (Fig. 9b), and this is consistent with the decreasing mean pressure (Fig. 7a) that attains its minimum at $x/c \approx 0.77$. Downstream of the pressure minimum, the controlled reverse flow region begins to diminish, while simultaneously the baseline reverse flow region increases such that at $x/c = 0.85$ (Fig. 9c) their reverse flow regions are approximately the same. This corresponds approximately to the C_p crossover at $x/c = 0.83$ shown in Fig. 7a. Further downstream, the larger pressure recovery rate associated with the controlled case (Fig. 7a) is consistent with the rapidly attaching boundary layer (Fig. 9d) and reattachment at

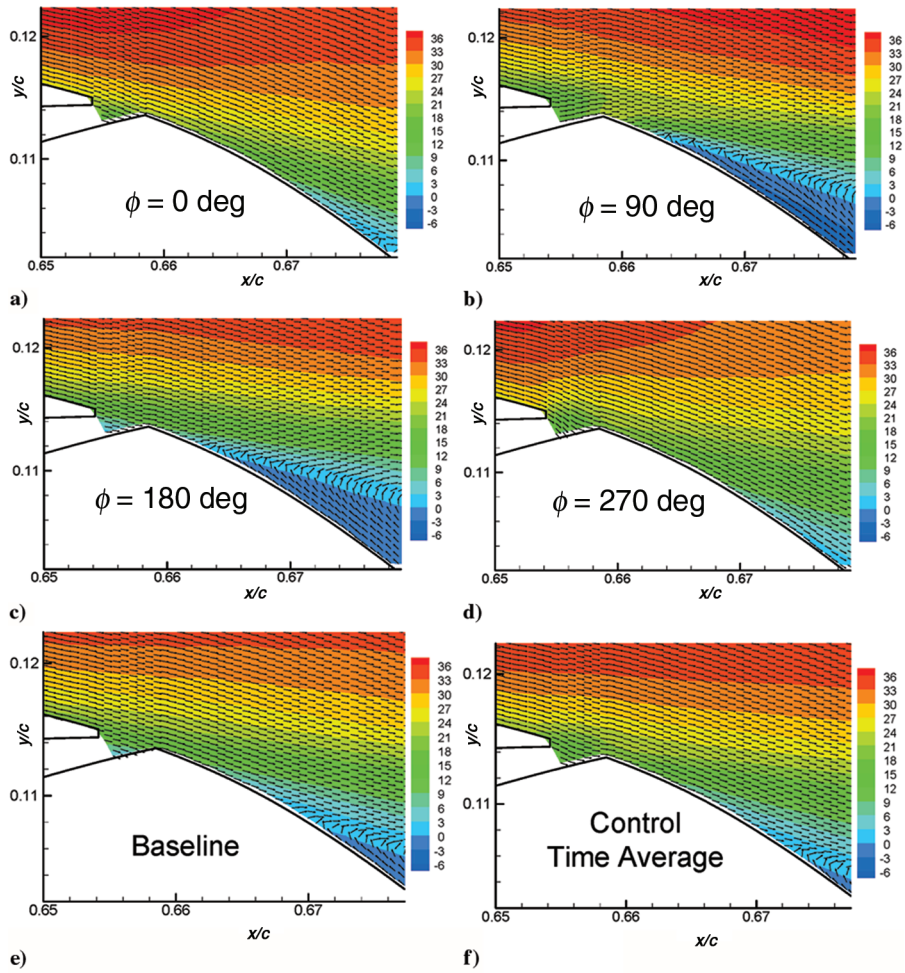

Fig. 10 Phase-averaged streamwise velocity contours (m/s) and normalized $\langle u\rangle$–$\langle v\rangle$ vectors for indicating flow direction at four phases of the control cycle corresponding to zone 1 in Fig. 3 ($0 < \phi < 180$ deg—blowing phase; $180 < \phi < 360$ deg—suction phase). Also, corresponding baseline and time-mean control data.

$x/c = 0.98$. In contrast, steady suction produces a larger momentum increase in the outer layer, without the intensified reverse flow region, and reattachment at $0.92 \leq x/c \leq 0.94$ (see Part 1 [3]).

The time-mean behavior shown in Figs. 7–9 was further elucidated with respect to phase-averaged measurements in the near vicinity of the slot [zone 1; selected phases are shown in Figs. 10a–10d; normalized vectors (flow direction) are plotted together with contours of the U-component of velocity]. $\phi = 90$ deg was chosen to correspond to the peak-blowing velocity such that $0 \leq \phi \leq 180$ deg and $180 < \phi < 360$ deg represent the blowing and suction phases, respectively. This represents a shift of 80 deg when compared with the data referred to [2]. At the transition between the blowing and suction phases ($\phi = 0$ deg), the shear layer is drawn relatively close to the model surface upstream of the slot (Fig. 10a). On the ramp downstream of the slot, the separation point can also be discerned at $x/c \approx 0.677$. As the slot blowing amplitude increases, the separation point progresses *up the ramp* and at the phase corresponding to the blowing peak, separation has progressed to $x/c \approx 0.664$ with the shear layer deflected away from the wall (Fig. 10b). The velocity vectors between the slot and separation point are pointing away from the wall and the velocity upstream of the slot is retarded. As the blowing amplitude diminishes, upstream velocity remains retarded and the separation point does not move significantly, although the near-wall velocities increase (Fig. 10c). With the commencement of the suction phase, the separation point moves rapidly downstream and halfway through the suction cycle, the separation point has moved out of the field of view shown here ($x/c > 0.68$; Fig. 10d), velocity vectors are tangent to the ramp wall, and high velocity flow is established upstream of the slot.

These measurements illustrate to some degree the mechanism behind the time-mean observations discussed with respect to zero mass-flux control: the blowing and suction phases tends to alternately promote and reduce separation close to the slot, respectively. In a similar fashion, the near-wall velocity upstream of the slot alternately increases and decreases depending on the phase with a small net result (cf. Figs. 10e and 10f). This accounts for the lack of a "suction peak" upstream of the slot such as that observed when control is applied by means of steady suction alone (Fig. 7a). Although the detrimental pressure drop downstream of the slot seems counterintuitive (Fig. 7a), there is a precedent in the application of boundary layer control (BLC) by steady blowing [17]. When steady control is applied upstream of separation with $U_J/U_\infty < 1$ the jet serves to retard the boundary layer flow resulting in lower near-wall momentum and hence a boundary layer that is more susceptible to separation. A threshold slot velocity ratio $U_J/U_\infty \sim 1$ must be reached before a positive net effect, such as an increase in lift, is observed. Consequently, a steady blowing net momentum coefficient was proposed [17]:

$$C_{\mu,\text{net}} = (1 - U_\infty/U_J) \times C_\mu \equiv C_\mu - 2C_Q \tag{14}$$

which correlated well with airfoil data. In this zero mass-flux control experiment, as well as some others, a similar mechanism may be at work. For example, in many low-speed investigations, model or airfoil slot width to chord ratios are within the range $0.1\% < b/c < 0.3\%$. From the definition shown in Eq. (3), this corresponds to the same C_μ range when $u_p/U_\infty = 1$, and many investigations cite a threshold C_μ in this range above which zero mass-flux separation control becomes effective [1]. Using a similar argument to that presented earlier in this paper [17], we can express a net zero mass-flux momentum coefficient as

$$C_{\mu,\text{net}} = (1 - U_\infty/u_p) \times C_\mu \equiv C_\mu - \sqrt{2}C_{Qp} \tag{15}$$

where $C_{Qp} = bu_p/cU_\infty$. Care should be exercised when applying Eq. (15) to a zero mass-flux case because in some instances performance enhancements are observed with $C_{\mu,\text{net}} < 0$! This is because, unlike steady BLC, the shear layer instability and subsequent rollup of LCSs can play a dominant role in determining the separation control attributes (see discussion in the next section). Note that a case can be made for the superposition of a net positive (blowing) [9] or negative (suction) [1,5] mass-flux to enhance separation control effectiveness: positive mass-flux increases the near-wall momentum but the shear layer is more stable; negative mass-flux decreases near-wall momentum but the shear layer is more unstable.

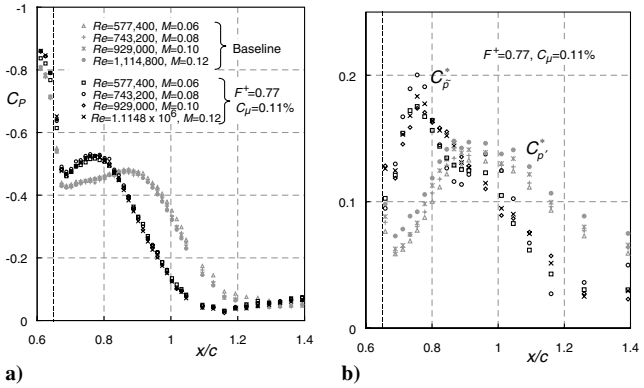

Fig. 11 Effect of Reynolds number on a) mean and b) fluctuating surface pressures (vertical line indicates slot location).

C. Effect of Reynolds Number, Control Frequency, & Control Amplitude

Time-mean and unsteady pressure data described in the preceding section were found to be almost completely independent of Reynolds number for the range considered here (Figs. 11a and 11b). Note that each control case required a different physical frequency and amplitude to achieve the same reduced conditions (see Sec. IV and Fig. 5). Although the Reynolds number range presented here is small, a larger effect was discerned with respect to steady-suction data for the same Reynolds number range [3]. A further explanation for the present small Reynolds number effect is discussed later in this paper which cites saturation of control authority. Like [3], this data set together with the cryogenic setup [5] facilitated an assessment of Reynolds number effects without the usual complications associated with transition and compressibility. A comparison at the test condition (Fig. 12) shows a significant difference in the effectiveness of control at the different Reynolds numbers. Differences were also observed under control by steady suction [3]. Although the slot geometries are slightly different, it is unlikely that the observed differences are due to these geometric effects alone.

The effect of increasing C_μ on surface pressures at the test case frequency can be seen in Figs. 13a–13d, and Fourier amplitudes for low and high C_μ are shown in Figs. 14a and 14b. Based on these data, separation control can be characterized differently for "low" and "high" C_μ, respectively. For low C_μ, perturbations reduce the overall bubble length, as can be seen from the pressure recovery, but the

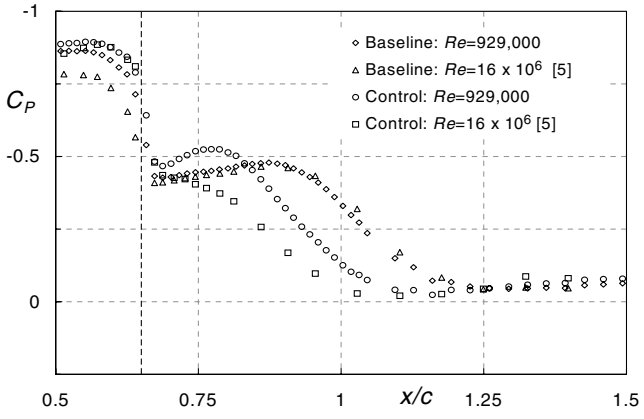

Fig. 12 Comparison of atmospheric and cryogenic data sets at the test case condition representing a factor of 16 difference in Reynolds number. Control at $F^+ = 0.77$; $C_\mu = 0.11\%$.

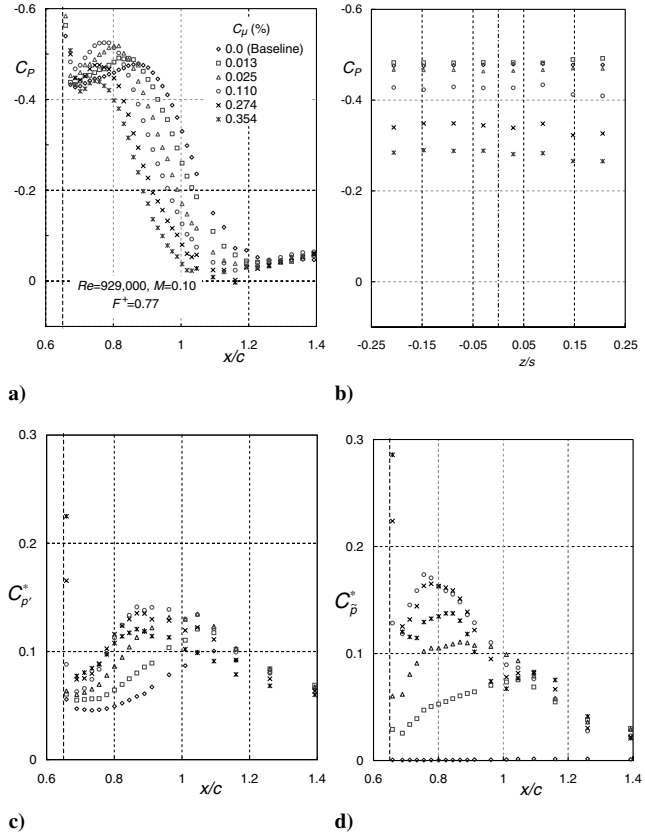

Fig. 13 a) Mean streamwise, b) mean spanwise, c) turbulent rms, and d) coherent rms pressure coefficients for various control amplitudes at the test case reduced frequency.

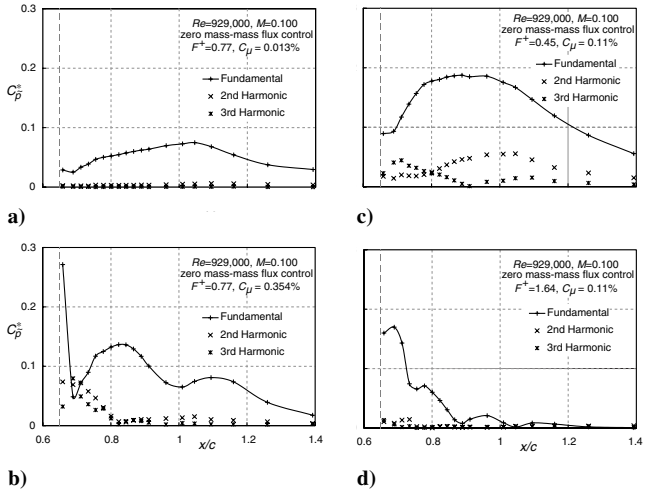

Fig. 14 Fourier amplitudes of the coherent pressure fluctuations for a) low and b) high C_μ at the test F^+ and c) low and d) high F^+ at the test C_μ.

reverse flow velocities downstream of the slot increase as is evidenced by the level and location of the low pressure region. This process of strengthening (lower mean C_P) and shortening the bubble continues with increasing C_μ, but saturates at $C_\mu \approx 0.11\%$, which coincidentally corresponds to the test case discussed earlier in this paper. The relative insensitivity to C_μ in this range may also be responsible for masking Reynolds number effects (see Fig. 11a). Increasing C_μ results in increased coherent and random pressure fluctuations (Figs. 13c and 13d), which typically achieve their peak values closer to the slot as C_μ increases. For low-amplitude perturbations ($u_p < U_\infty$; $C_\mu < 0.19\%$), the fundamental pressure

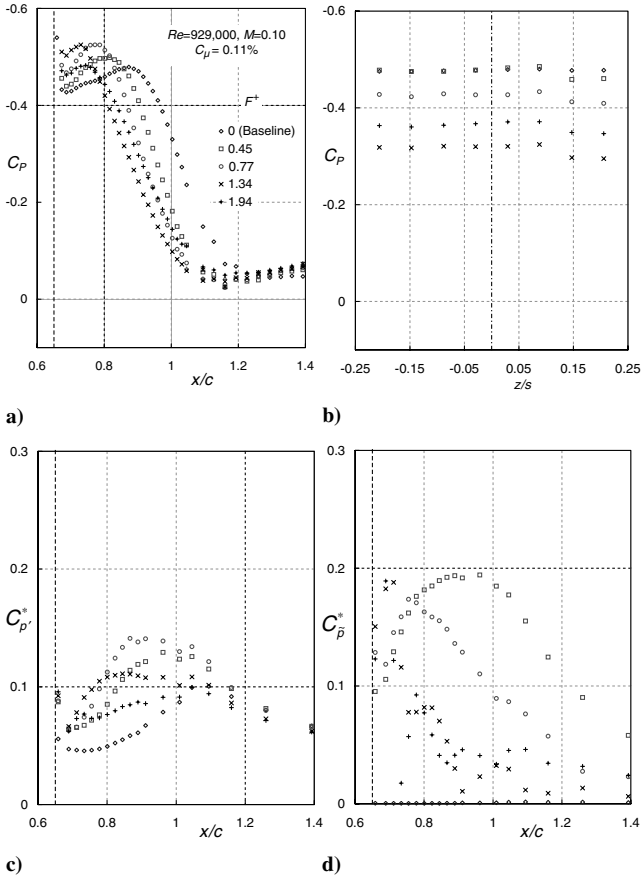

Fig. 15 a) Mean streamwise, b) mean spanwise, c) turbulent rms, and d) coherent rms pressure coefficients for various control frequencies at the test case reduced amplitude.

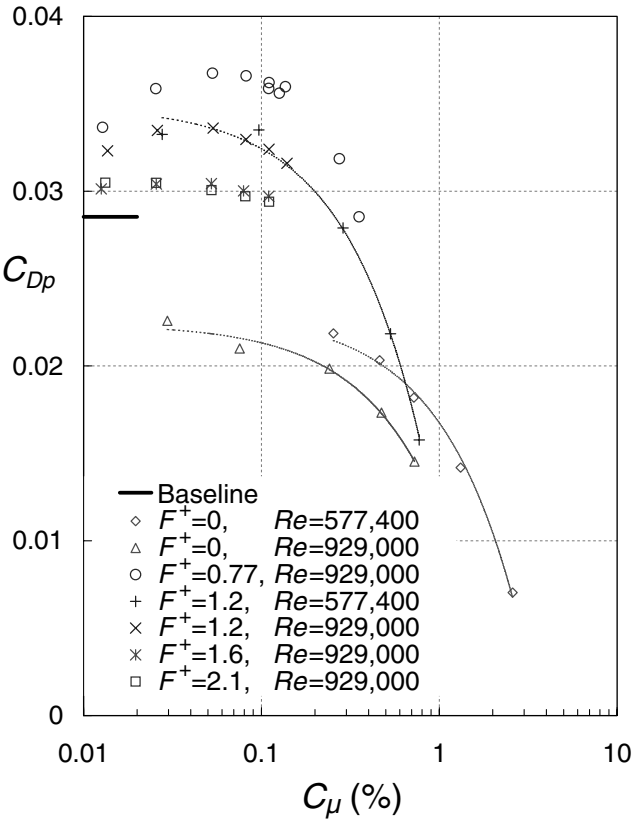

Fig. 16 Comparison of the form-drag coefficient for zero mass-flux and steady suction on the basis of C_μ.

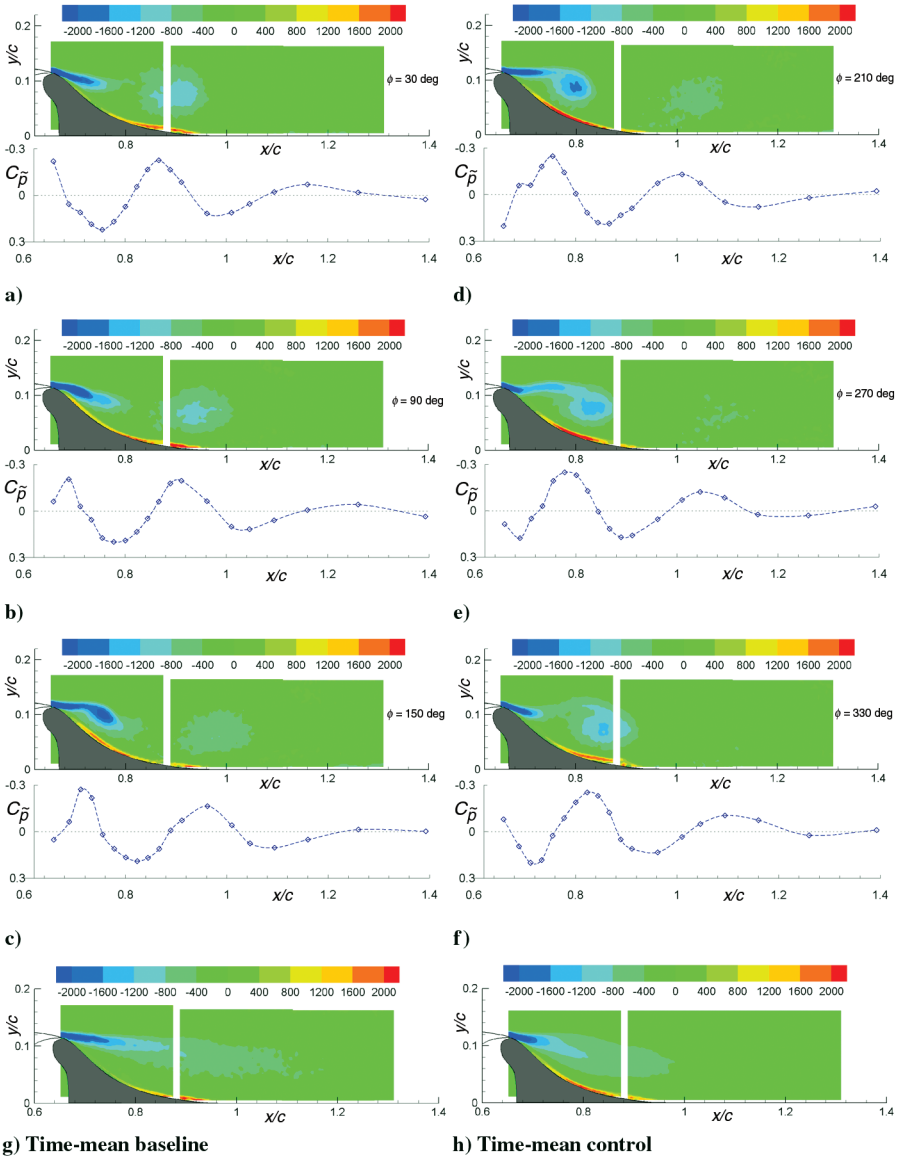

Fig. 17 a–f) Phase-averaged spanwise vorticity field $\langle\omega_z(x, y, t)\rangle$ with corresponding coherent surface pressure fluctuations $C_{\tilde{p}} = \langle C_P\rangle - C_P$ at six phases of the control cycle; g) baseline and h) corresponding control time mean.

fluctuation dominates throughout the separated and reattached flow regions (Fig. 14a). For $C_\mu > 0.19\%$, forcing begins to diminish the mean strength of the bubble, as can be seen by the higher C_P, whereas the overall bubble length continues to shorten. In addition, $C^*_{p'}$ and $C^*_{\tilde{p}}$ saturate and their amplitudes decrease relative to the fluctuation amplitudes at the lower edge of the slot (left-most data points), which we consider to be the fluctuating pressure "boundary conditions" (see Sec. III and Fig. 2). For $u_p > U_\infty$, the harmonic content is comparable to the fundamental near the slot ($x/c < 0.75$), but diminishes readily downstream (Fig. 14b). The nonmonotonic decay of fundamental wave appears when $u_p > U_\infty$ (see Fig. 14b). Flowfield measurements will be required to further understand the source of the nonmonotonic decay.

The C_μ range corresponding to saturation of the bubble strength ($-C_P$ downstream of the slot) and pressure fluctuations may be considered to be a transition range approximately demarcating low- and high-amplitude control. The surface pressure fluctuations are proportional to the strength of the spanwise momentum-transferring vortices (see Figs. 17a–17f) and thus it may be conjectured that the low-amplitude perturbations rely predominantly on excitation of the free-shear layer to effect separation control. With high-amplitude control, separation control relies more on alternately adding momentum via blowing and removing the boundary layer during suction, and it is less clear how much high-amplitude forcing of the shear layer contributes. For the present setup $u_p \approx U_\infty$ can be considered a reasonable approximation of the transitional point between low- and high-amplitude separation control. Similar observations were made at various reduced frequencies in the range $0.45 \le F^+ \le 1.94$. In the present case, a pressure recovery immediately downstream of the slot is only evident when $C_\mu \approx 0.35\%$, but this value is somewhat dependent on F^+ as will be shown later in this paper. The asymmetry associated with the pressure recovery (Fig. 13b) over the central part of the model ($-0.25 \le z/s \le 0.25$) is believed to be due to the momentum asymmetry introduced as a result of the small spanwise slot variation described in Sec. IV.C.

The effect of increasing the reduced frequency F^+ at constant C_μ is shown in Figs. 15a–15d for selected cases and Fourier amplitudes for low and high F^+ are shown in Figs. 14c and 14d. At low control frequencies ($F^+ < 1$) increasing the frequency has a similar effect to that of increasing C_μ, namely, the near-wall reverse flow region intensifies but the reattachment length reduces. A decrease in pressure downstream of the slot is accompanied by an improved pressure recovery further downstream. However, an optimum frequency is reached where the shortest pressure recovery occurs at $1.05 \le F^+ \le 1.35$; this corresponds approximately to that associated with attaching a separated shear layer to a deflected flap using small C_μ [16]. With further increases in F^+ this mean pressure

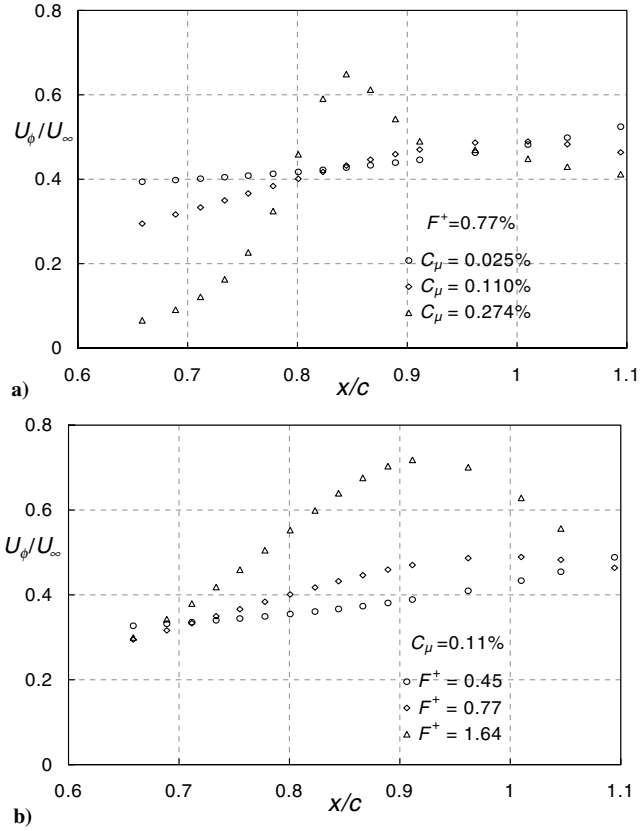

Fig. 18 Vortex speed estimates for a) varying C_μ at the test F^+ and b) varying F^+ at the test C_μ.

trend reverses, i.e., pressure drop immediately downstream of the slot is smaller, but the recovery is adversely affected near reattachment. At low and high frequencies the fundamental perturbations dominate (Figs. 14c and 14d). At the lower frequency ($F^+ = 0.45$, Fig. 14c), the amplification and dissipation of the perturbation is more gradual than at the test condition and still significant well downstream of the baseline reattachment point. The second and third harmonics, although relatively small, attain larger values than those at other frequencies and amplitudes. At the higher frequency ($F^+ = 1.64$), highly nonmonotonic behavior is evident, with no fewer than four distinct peaks visible. The amplification of the pressure fluctuations is dramatically affected by changes in frequency. The highest levels of turbulent and coherent pressure fluctuations occur for $F^+ = 0.77$ and 0.45, respectively, (Figs. 15c and 15d), which is somewhat less than the optimum for separation control. At frequencies higher than the optimum F^+, turbulent pressure fluctuations show a net decrease when compared with their value at the lower slot edge. Coherent fluctuations always amplify at some distance downstream of the slot, and with increasing frequency they 1) attain their peak values closer to the slot, 2) decay over a successively shorter distance, and 3) exhibit large amplitude variations. It is evident that the shear layer stability also plays a defining role in the transfer of momentum from the freestream to the wall. To adequately predict the effect of control, both the slot effect (Sec. V.B) and the shear layer instability must be properly accounted for.

Typically, a somewhat smaller C_μ is required to eliminate the separation bubble on a flap [16] or airfoil [9] than that required to eliminate the bubble in the present investigation. A possible explanation is that, in the present case, fluid can only be entrained from the "dead air" region between the shear layer and the wall (ramp faired into the splitter plate). In the case of an airfoil or flap, the low pressure generated by separation control causes additional entrainment of fluid from below the airfoil or flap surface.

The effect of control amplitude and frequency on C_{Dp} is summarized in Fig. 16; the baseline value is indicated on the ordinate. The process of strengthening and shortening the bubble

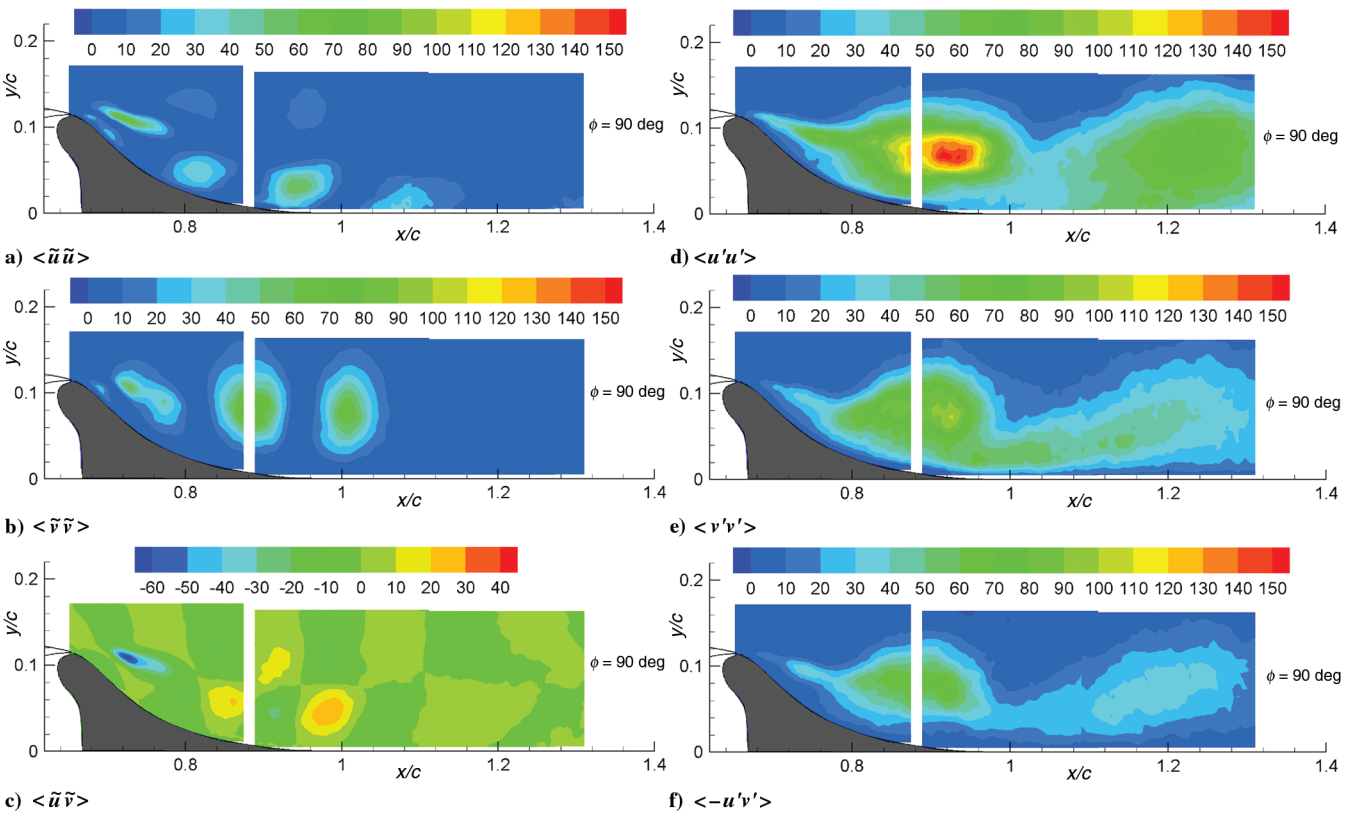

Fig. 19 Phase-averaged coherent and turbulent Reynolds stresses at $\phi = 90$ deg (all data in m^2/s^2).

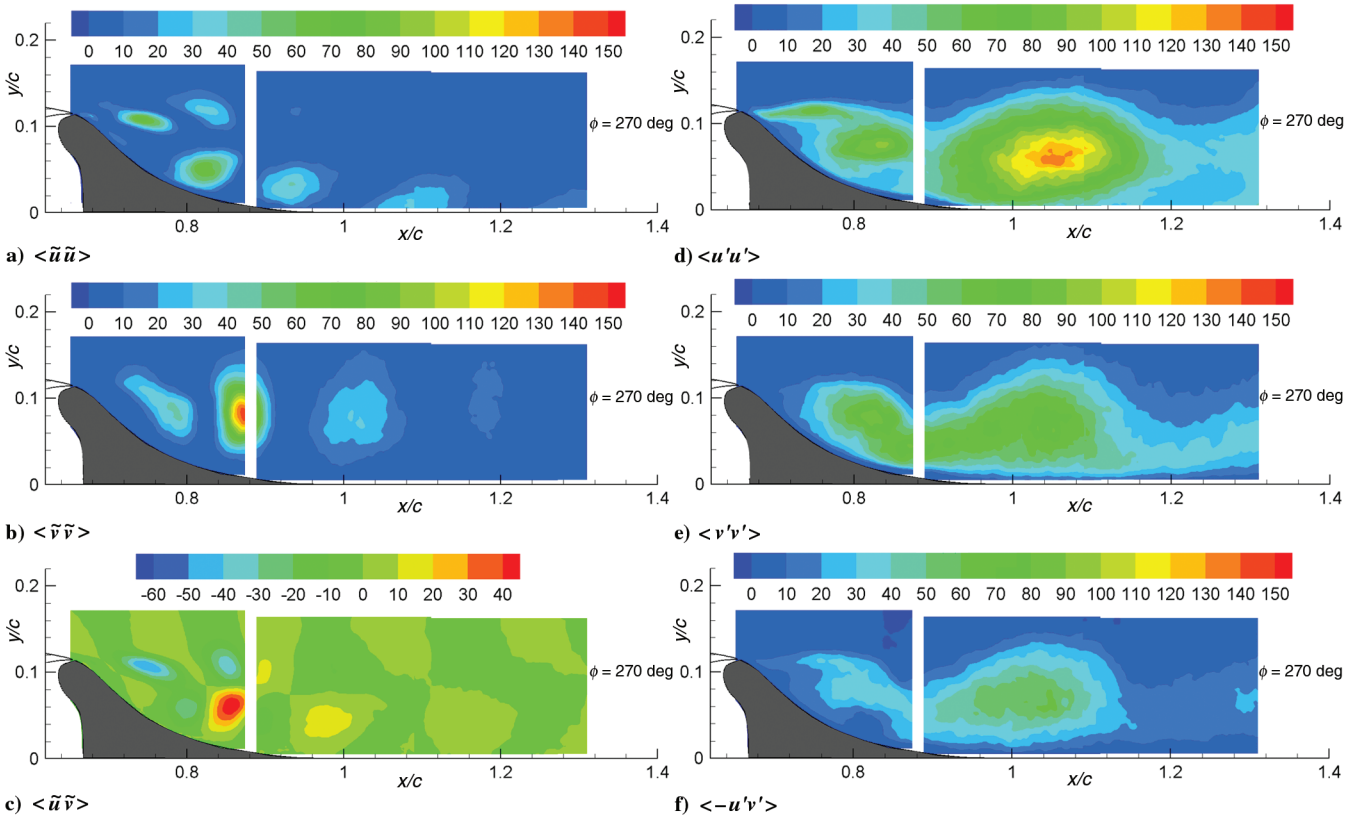

Fig. 20 Phase-averaged coherent and turbulent Reynolds stresses at $\phi = 270$ deg (all data in m^2/s^2).

(lower C_P downstream of the slot) with increasing C_μ manifests as a form-drag *increase* at low C_μ. At higher frequencies, where the bubbles are weaker, the drag increase is smaller. Higher amplitude control achieved at lower Reynolds numbers resulted in further ramp pressure increases immediately downstream of the slot and a net decrease in C_{Dp} that was only observed at C_μ corresponding to $u_p/U_\infty > 1$. Steady suction ($F^+ = 0$), on the other hand, always increases the ramp pressure as is evident in Fig. 16 and is clearly more effective than zero mass-flux control for reducing drag at low C_μ on this model. However, at frequencies close to optimum for separation control (presently $F^+ = 1.2$), there is a crossover C_μ at high amplitudes, where zero mass-flux control becomes more effective.

D. Shear Layer Excitation

The generation, rollup, and shedding of the vortex for the oscillatory test case is described with respect to Figs. 17a–17f, which show the simultaneous phase-averaged spanwise vorticity field ($\langle\omega_z\rangle = \partial\langle v\rangle/\partial x - \partial\langle u\rangle/\partial y$) and the coherent phase-averaged surface pressures $C_{\tilde{p}}$ at six phases. Soon after the start of the blowing phase ($\phi = 30$ deg; Fig. 17a) the shear layer downstream of the slot is deflected downward towards the model surface. This feature is an artifact of the suction cycle that preceded the blowing cycle (discussed later in this paper with respect to Fig. 17f). A previously generated vortex is centered at $x/c \approx 0.9$ and corresponds approximately to a local pressure minimum. The

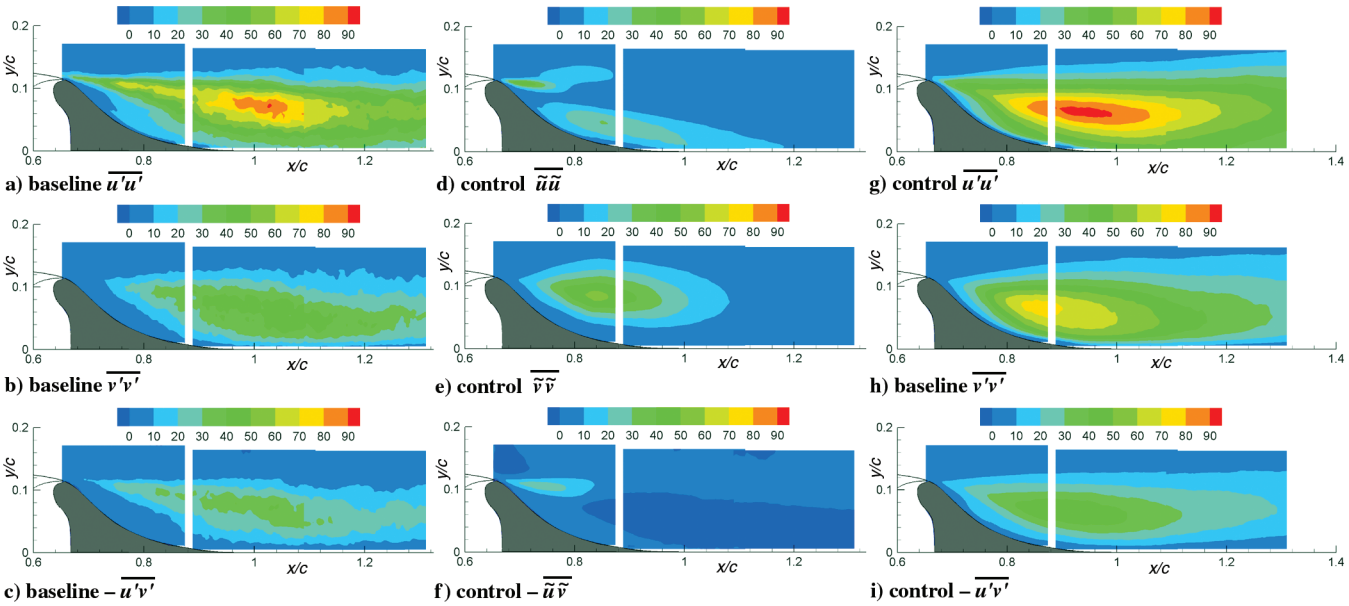

Fig. 21 Time-mean baseline Reynolds stresses and time-mean coherent and turbulent Reynolds stresses (all data in m^2/s^2).

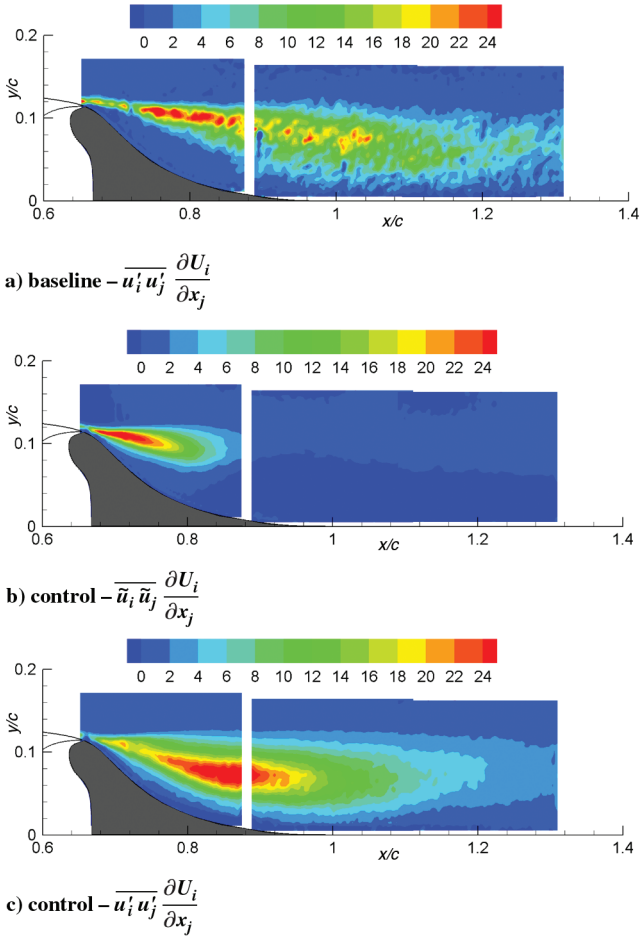

Fig. 22 Energy fluxes from the mean flow to the coherent and turbulent components (all data in m^2/s^3).

region of high positive vorticity close to the wall, underneath the vortex, is indicative of the extent and magnitude of the near-wall reverse flow. A region of weaker vorticity also exists at $1.05 \lesssim x/c \lesssim 1.25$, corresponding to the mild local pressure minimum, but it cannot be seen on the present scale.

As the blowing increases to its peak value ($\phi = 90$ deg; Fig. 17b) the shear layer just downstream of the slot lifts off the wall, and becomes distorted. The region of reverse flow now exits over virtually the entire ramp commencing at $x/c \approx 0.664$ (cf. Figs. 10b and 17b). This distorted shear layer characterizes the early stages of vortex rollup and is associated with a pressure minimum just downstream of the slot. At this phase, three distinct pressure minima are present, corresponding approximately to the three vortices existing simultaneously in the measured flowfield. As the blowing amplitude diminishes ($\phi = 150$ deg; Fig. 17c), the vortex becomes more pronounced, convects downstream and induces a region of larger positive vorticity (reverse flow) near the wall as a consequence of the no-slip condition. As the control switches from blowing to suction ($\phi = 210$ deg; Fig. 17d), the vortex begins to break away from the shear layer. The distinct shear layer and vortex coexisting produce the nonlinear pressure response shown in the upstream pressure ports. In the middle of the suction phase ($\phi = 270$ deg; Fig. 17e), the shear layer is drawn close to the wall near the slot and develops a kink, although the vortex is not fully shed from the shear layer. Toward the end of the suction cycle, the vortex breaks free and convects downstream (Fig. 17f).

The distance between negative pressure peaks is indicative of the spacing between the vortices, and reflects the increasing phase velocity (U_ϕ) of each vortex as it is generated and convected downstream. Pressure minima indicate that the vortex speed close to the slot is inversely proportional to C_μ (Fig. 18a). Vortices all accelerate downstream, with acceleration rate proportional to C_μ. At low C_μ maximum vortex speed is attained in the vicinity of reattachment. At high C_μ acceleration is rapid with maximum velocity at $x/c \approx 0.85$ followed by a relatively rapid deceleration. Vortex acceleration rate close to the slot is also proportional to F^+ with maximum velocities occurring successively closer to the slot (Fig. 18b).

E. Coherent & Turbulent Statistics

Phase-averaged coherent and turbulent Reynolds stresses are shown for the peak-blowing phase ($\phi = 90$ deg; Figs. 19a–19f) and at the middle of the suction phase ($\phi = 270$ deg; Figs. 20a–20f). The coherent generation and shedding of the separation control vortices produce regions or "islands" of relatively high coherent stresses. The wavelength between typical regions in the downstream direction is approximately half of the wavelength between successive vortices. As expected, the coherent stresses dissipate relatively quickly in the downstream direction. Figures 19d–19f and 20d–20f show the extent to which the coherent motion also organizes the turbulent Reynolds stresses into concentrated regions. These correspond approximately to the regions of high vorticity that are associated with the rolled up vortices (see Figs. 17b–17e), where local peak values of $\langle u'u' \rangle$ exceed $-\langle u'v' \rangle$ and $\langle v'v' \rangle$ by a factor of about 2. The stresses involving $-\langle \tilde{u}\,\tilde{v} \rangle$ show both negative and positive values (Figs. 19c and 20c; note the different scale). The reason for the unusual

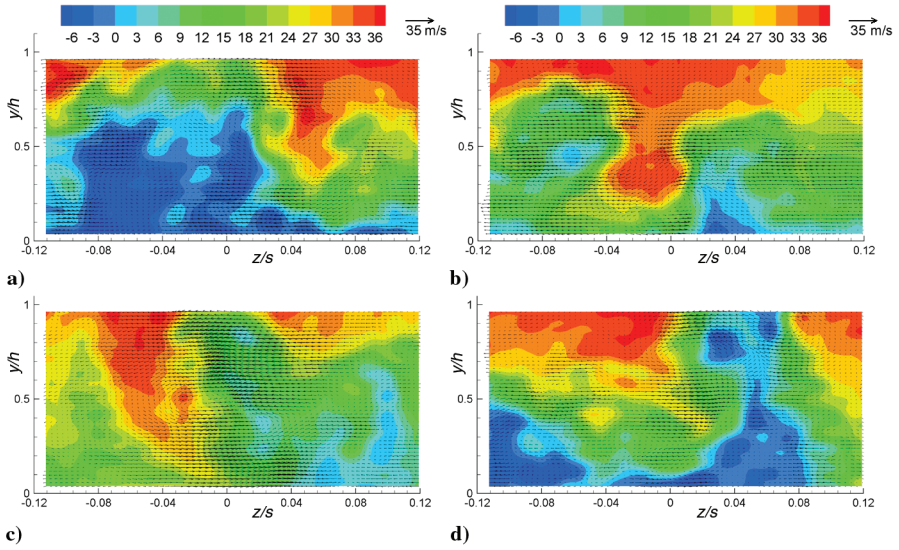

Fig. 23 Four examples of instantaneous velocities at $x/c = 1.0$ and $\phi = 60$ deg. Contours are the u-component; vectors are v–w (all data in m/s).

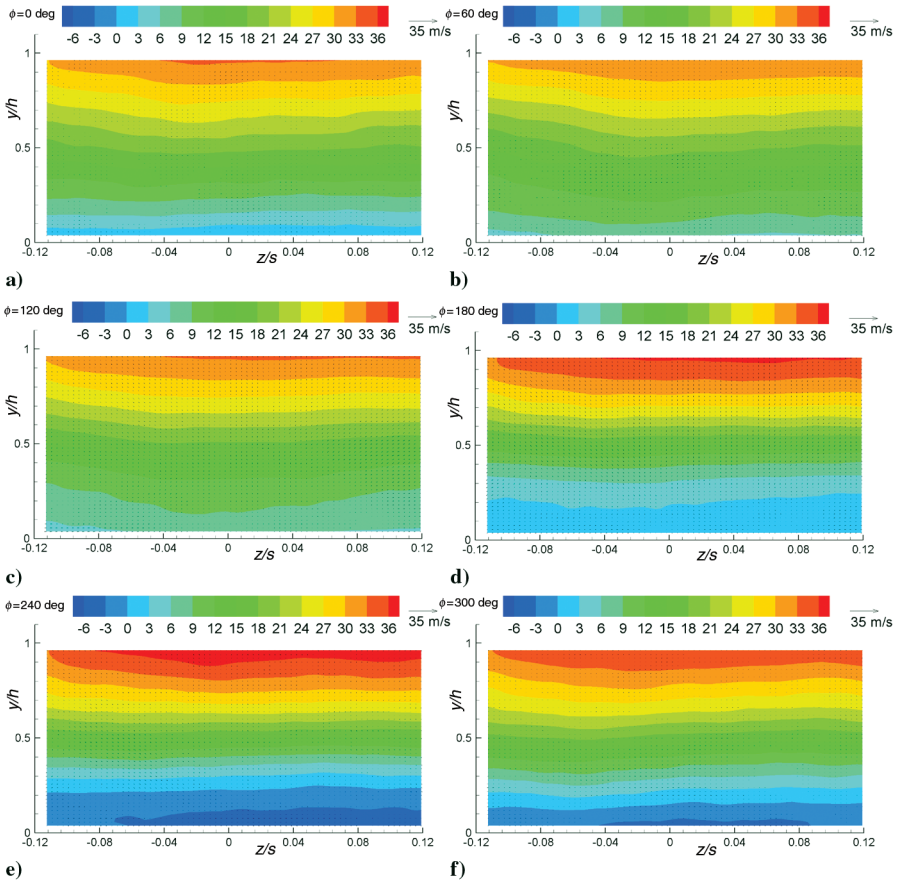

Fig. 24 Phase-averaged velocities for six phases at $x/c = 1.0$. Contours are the u-component; vectors are v–w (all data in m/s).

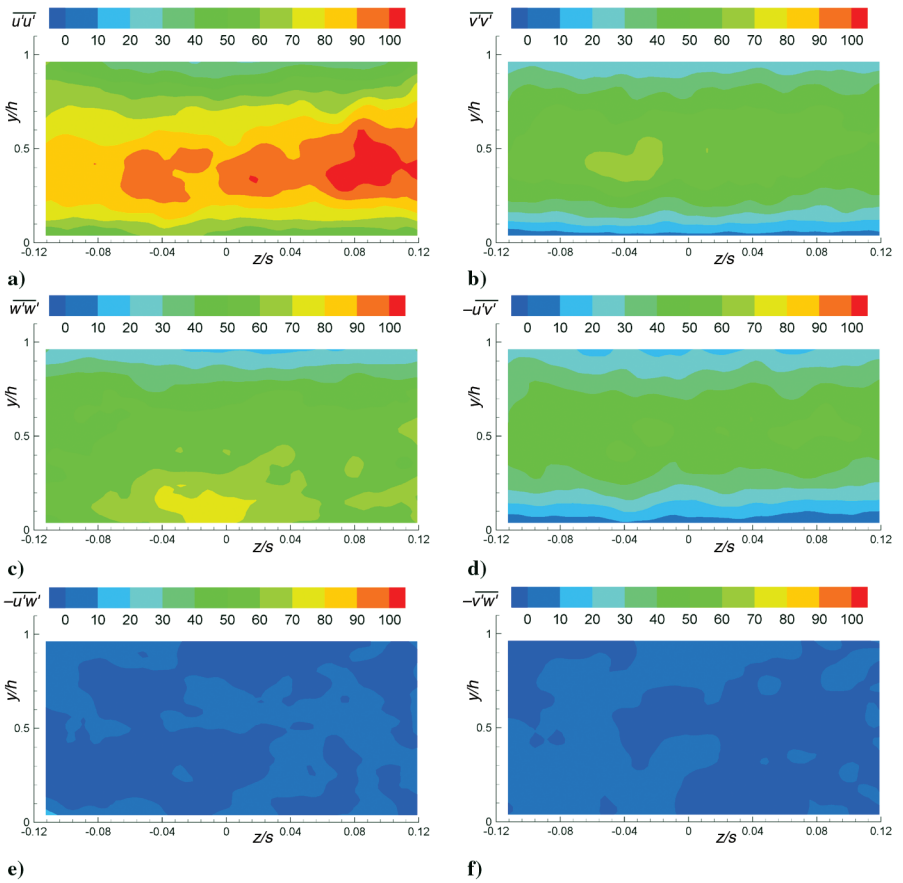

Fig. 25 Phase-averaged Reynolds stresses at $x/c = 1.0$ and $\phi = 0$ deg (all data in m^2/s^2).

$-\langle\tilde{u}\,\tilde{v}\rangle < 0$ is that localized positive $\tilde{u}$ and $\tilde{v}$ (during the blowing cycle) and negative $\tilde{u}$ and $\tilde{v}$ (during the suction cycle) occur simultaneously. The triple decomposition makes clear that this does not arise from the turbulence supplying energy to the mean flow, but rather the interaction of the coherent oscillations in the flow. It will be noted later in this paper (see Fig. 21f) that in a time-mean sense the term $-\overline{\tilde{u}\,\tilde{v}} > 0$ throughout the flowfield, indicating a net transfer of energy from the mean to the coherent motion. It is therefore concluded that these features do not arise as a result of so-called vortex nutation [18] where the orientation of the vortex gives rise to a net transfer of energy to the mean flow.

Time-averaged data resulting from the triple decomposition is useful for understanding how the perturbations produce and spatially organize the turbulence [11,12]. It also allows comparison of the relative magnitudes and spatial distribution of the coherent and turbulent stresses. The time-averaged baseline turbulent stresses and control coherent and turbulent stresses are shown in Figs. 21g–21i, respectively. As a general rule, the coherent stresses attain their largest values close to excitation slot where the coherent perturbations are most significant. For example, the concentrated $\overline{\tilde{u}\,\tilde{u}}$ near the slot and its proximity to the surface (nearly normal to the surface) is consistent with the large $C_{\bar{p}}^*$ at the wall. Although positive values of $\langle\tilde{u}\,\tilde{v}\rangle$ are observed at various phases of the control cycle (see Figs. 19c and 20c), they do not emerge as a dominant feature in a time-averaged sense. The relatively large turbulent stresses associated with control and their distribution within the flowfield is consistent with the magnitude and distribution of the turbulent pressure fluctuations $C_{p'}^*$ (e.g., Fig. 7b).

Energy flux from the mean flow to the coherent and turbulent fields (Figs. 22a–22c)

$$-\overline{\tilde{u}_i\tilde{u}_j}\frac{\partial U_i}{\partial x_j} \quad \text{and} \quad -\overline{u_i'u_j'}\frac{\partial U_i}{\partial x_j}$$

can also be calculated from the mean flow statistics (for convenience, the common subscripted variable shorthand is used here) [11,12]. These data clearly show how separation control results in significant coherent energy transfer near the slot, but further downstream this is superseded almost entirely by energy transfer to the turbulent motion.

F. Flowfield Two-Dimensionality

Aspects of the flow two-dimensionality were considered previously from the perspective of the model geometry [3], slot perturbations (Sec. IV.C) and spanwise pressures on the ramp (Sec. V.C). In this section flowfield two-dimensionality was considered by means of stereo PIV measurements, in planes $x/c = 0.7$ (close to the slot) and $x/c = 1.0$ (in the vicinity of time-mean reattachment line) extending over the spanwise distance $-0.12 \le z/s \le 0.12$. Phase-averaged velocity fields at $x/c = 0.7$ showed effectively two-dimensional flow (not shown). Examples of the three instantaneous velocity components (u, v, w) near reattachment ($x/c = 1.0$) at a single phase ($\phi = 60$ deg) are shown in Figs. 23a–23d. These instantaneous fields were chosen specifically to illustrate large excursions from the phase-averaged velocity field. Despite the effectively two-dimensional perturbations, the instantaneous velocity field is highly three-dimensional with instantaneous velocity components of similar magnitude. For the streamwise velocity component, localized reversed flow regions penetrate well into the boundary layer (to approximately the height of the model, $y/h \approx 1$), and in-plane $\sqrt{v^2 + w^2}$ velocities are as large as $0.8U_\infty$. The streamwise vortical structures have a maximum size and spacing that is approximately $h/2$. Phase-averaged streamwise velocities ($\langle u\rangle$, $\langle v\rangle$, $\langle w\rangle$) for six phases are shown in Figs. 24a–24f. It is evident that the highly three-dimensional flow has no preferred time-mean structure. The spanwise variations and cross-stream velocity components are on the order of the error associated with the PIV measurement (i.e., $0.03U_\infty$; see [3] for more details).

Phase-averaged turbulent statistics also indicate substantial flow two-dimensionality as shown in the example of the six Reynolds stress components shown at $\phi = 0$ deg (Figs. 25a–25f). The relatively large $\langle u'u'\rangle$ with respect to $-\langle u'v'\rangle$ and $\langle v'v'\rangle$ is consistent with the two-dimensional PIV data discussed in Sec. V.E. Despite the large instantaneous structures present in the flow (Figs. 23a–23d), w' is virtually uncorrelated with either u' or v' (Figs. 25e and 25f). This might serve as justification for modeling the flow using two-dimensional (e.g., URANS-type) approaches [2]. The absence of flow three-dimensionality may be due to the boundary layer reattachment beyond the concave ramp. For boundary layers developing on curved surfaces, the surface curvature is expected to generate streamwise vortices resulting from a centrifugal instability. Nevertheless, these vortices may meander and hence their presence may not be obvious when simple ensemble averaging is used. Their presence, however, affects the momentum transfer across the flow and is thus an important and sometimes dominant component in understanding and controlling such flows.

VI. Concluding Remarks

This paper summarized the second part of a CFD validation study of separation control over a wall-mounted hump by means of two-dimensional zero mass-flux perturbations. The main effort was expended in documenting a single control case that comprised static surface pressures together with phase-averaged dynamic surface pressures and PIV flowfield measurements. Due consideration was given to characterizing the flow in the vicinity of the control slot, with and without external flow, and establishing perturbation two-dimensionality. Spanwise surface pressures and phase-averaged stereoscopic PIV data revealed an effectively two-dimensional flowfield despite highly three-dimensional instantaneous flow structures. The test case is expected to be particularly challenging for CFD codes because different, sometimes counteracting, mechanisms dominate the separated flowfield during different parts of the control cycle.

Acknowledgments

This work was performed while the first author held a National Research Council–NASA Langley Research Center Associateship. The authors wish to thank W. L. Sellers III, M. J. Walsh, A. E. Washburn, N. W. Schaeffler, A. Seifert (Tel Aviv University), L. P. Melton, M. A. Kegerise, C. L. Rumsey, T. B. Gatski, and P. Balakumar for their assistance and many insightful suggestions. Detailed design and construction of the actuator by J. Kiedaisch, H. Nagib, and their associates from IIT contributed immensely to the data quality, two-dimensionality, and long-term repeatability of the experimental data. The authors also wish to thank R. L. Clark, R. S. Geouge, T. E. Fowler, and M. Bell for their excellent technical support.

References

[1] Greenblatt, D., and Wygnanski, I., "Control of Separation by Periodic Excitation," *Progress in Aerospace Sciences*, Vol. 37, No. 7, 2000, pp. 487–545.

[2] Rumsey, C., Gatski, T., Sellers, W., Vatsa, V., and Viken, S., "Summary of the 2004 CFD Validation Workshop on Synthetic Jets and Turbulent Separation Control," AIAA Paper 2004-2217, June–July 2004; (also see cfdval2004.larc.nasa.gov/case3.html).

[3] Greenblatt, D., Paschal, K., Yao, C., Harris, J., Schaeffler, N., and Washburn, A., "Experimental Investigation of Separation Control Part 1: Baseline and Steady Suction," *AIAA Journal* (to be published); also AIAA Paper 2004-2220, June–July 2004.

[4] Nagib, H., Kiedaisch, J., Wygnanski, I., Stalker, A., Wood, T., and McVeigh, M., "First-in-Flight Full-Scale Application of Active Flow Control: The XV-15 Tiltrotor Download Reduction," *Presented at the Research and Technology Organization AVT-111 Specialists' Meeting on Enhancement of NATO Military Flight Vehicle Performance by Management of Interacting Boundary Layer Transition and Separation*, Paper 29, Prague, Oct. 2004.

[5] Seifert, A., and Pack, L. G., "Active Flow Separation Control on Wall-Mounted Hump at High Reynolds Numbers," *AIAA Journal*, Vol. 40, No. 7, 2002, pp. 1363–1372.

[6] Seifert, A., and Pack, L. G., "Effects of Compressibility and Excitation Slot Location on Active Separation Control at High Reynolds Numbers," *Journal of Aircraft*, Vol. 40, No. 1, 2003, pp. 110–119.
[7] Poisson-Quinton, P., and Lepage, L., "Survey of French Research on the Control of Boundary Layer and Circulation," *Boundary Layer and Flow Control: Its Principles and Application*, edited by G. V. Lachmann, Vol. 1, Pergamon, New York, 1961, pp. 21–73.
[8] Schlichting, H., and Gersten, K., *Boundary Layer Theory*, 8th ed., Springer, Berlin, 2000, pp. 307–309.
[9] Seifert, A., Darabi, A., and Wygnanski, I., "Delay of Airfoil Stall by Periodic Excitation," *Journal of Aircraft*, Vol. 33, No. 4, 1996, pp. 691–698.
[10] Batchelor, G. K., *An Introduction to Fluid Dynamics*, Cambridge Univ. Press, Cambridge, England, U.K., 1967, pp. 88–90.
[11] Hussain, A. K. M. F., and Reynolds, W. C., "The Mechanics of an Organized Wave in Turbulent Shear Flow," *Journal of Fluid Mechanics*, Vol. 41, No. 2, 1970, pp. 241–258.
[12] Reynolds, W. C., and Hussain, A. K. M. F., "The Mechanics of an Organized Wave in Turbulent Shear Flow. Part 3. Theoretical Models and Comparisons with Experiments," *Journal of Fluid Mechanics*, Vol. 54, No. 2, 1972, pp. 263–288.
[13] Obi, S., Ishibashi, N., and Masuda, S., "The Mechanism of Momentum Transfer Enhancement in the Periodically Perturbed Turbulent Separated Flow," *2nd International Symposium on Turbulence, Heat and Mass Transfer*, edited by K. Hanjalíc and T. W. J. Peeters, Delft Univ. Press, Delft, The Netherlands, 1997, pp. 835–844.
[14] Coleman, H. W., and Steele, Jr., W. G., *Experimentation and Uncertainty Analysis for Engineers*, John Wiley and Sons, New York, 1989, Chaps. 2–3.
[15] Benedict, L. H., and Gould, R. D., "Towards Better Uncertainty Estimates for Turbulence Statistics," *Experiments in Fluids*, Vol. 22, No. 2, 1996, pp. 129–136.
[16] Nishri, B., and Wygnanski, I., "Effects of Periodic Excitation on Turbulent Separation from a Flap," *AIAA Journal*, Vol. 36, No. 4, 1998, pp. 547–556.
[17] Attinello, J. S., "Design and Engineering Features of Flap Blowing Installations," *Boundary Layer and Flow Control: Its Principles and Application*, edited by G. V. Lachmann, Vol. 1, Pergamon, New York, 1961, pp. 463–515.
[18] Ho, C., and Huerre, P., "Perturbed Free Shear Layers," *Annual Review of Fluid Mechanics*, Vol. 16, Jan. 1984, pp. 365–422.

R. Lucht
Associate Editor